Tribology in Industry

RESEARCH

Investigating Nanoindentation and Wear Properties of Spark Plasma Sintered Ti$_{48}$Al$_{48}$Cr$_2$Nb$_2$ Alloy

Mahlatse R. Mphahlele[a,b,*], Peter A. Olubambi[b,] Eugene Olevsky[c]

[a]*Department of Mechanical Engineering, Durban University of Technology, Durban, 4001, South Africa,*
[b]*Centre of Nanoengineering and Advanced Materials, School of Mining, Metallurgy & Chemical Engineering, University of Johannesburg, Doornfontein, 2094, South Africa,*
[c]*Powder Technology Laboratory, College of Engineering, San Diego State University, San Diego, CA, United States.*

A B S T R A C T

This work studied spark plasma sintered Ti$_{48}$Al$_{48}$Cr$_2$Nb$_2$ alloy for their nanoindentation and wear properties. Results showed an improvement in nanoindentation properties of the compacts with an increase in holding time from 5min to 7.5min for the heating rate of 50 °C/min and 100 °C/min. X-ray diffraction (XRD) analysis showed the intensity of diffraction peaks of two major crystalline phases of Ti$_3$Al$_{2.25}$Nb$_{0.75}$ and γ-TiAl. Scanning electron microscopy (SEM) images of sintered compacts possessed varied microstructures due to different sintering parameters. The nearly lamellar structure showed a good balance of yield stress and fracture toughness. Wear tracks SEM analysis revealed the worn surface morphologies and the sample sintered for 7.5 min at the eating rate of 50 °C/min sustained the least damage evident by the shallow grooves and narrow wear track. Profilometer measurements revealed the wear track depth and width, confirming the degree of wear for the samples sintered at varied conditions.

1. INTRODUCTION

Cutting-edge designs and structures in the aerospace and automobile industries continuously demand tailored advanced materials with superior engineering properties. Materials such as Titanium aluminide (TiAl) are excellent candidates as they offer a combination of properties of Ti and Al, such as excellent weight-to-ratio, high elastic modulus, flame resistance, and corrosion resistance [1]. Of late, the gamma (γ) – TiAl-based alloy, Ti$_{48}$Al$_{48}$Cr$_2$Nb$_2$, has attracted increasing relevance as an advanced structural material with outstanding properties than the traditional TiAl. Mainly, this is owed to the presence of minor fractions of chromium (Cr) and niobium (Nb), which are noted to enhance the ductility and stiffness of the TiAl alloys [2].

However, wider usage of TiAl alloys is yet to be realized as they are restricted by their low surface hardness and wear resistance. These limitations have rendered the alloys not suitable

for use in applications structural applications involving sliding contact [3]. Consequently, many researchers have devoted time and expertise to improving its wear resistance property using various methods, including surface modification, lubrication, reinforcement, and manufacturing processes [4].

Manufacturing processes such as additive manufacturing, hot isostatic pressing, combustion synthesis, spark plasma sintering, and laser technique have been applied to produce Ti-based alloys [5]. Interestingly, the novel spark plasma sintering (SPS) system has earned substantial momentum as an appealing fabrication tool to process titanium alloys with augmented properties, owing to its short processing time and relatively low temperatures [6]. Other added benefits of SPS include consolidation of powders through solid-state sintering or sometimes with only partial melting taking place; thus, it avoids the full melting of the metals and evolution of excessive intermetallic phases [7]. Furthermore, SPS affords seamless process control that enables the fabrication of Ti-based products with favourable microstructure containing limited imperfections [8]. Accordingly, the products have improved resistance to wear and failure when exposed to contact loading. This signifies that TiAl products with improved wear-resistance and mechanical properties can be attained by tailoring microstructure through manipulating process parameters via SPS. To ascertain the mechanical properties of TiAl, several traditional testing techniques, such as compression, tension, and impact tests have been utilized [9]. However, these methods are destructive and often require sizable samples for testing, making them unsuitable.

Nanoindentation is progressively gaining attention as an ideal method to probe the mechanical properties of materials due to its numerous benefits over traditional testing methods. It is a non-destructive method, and tests can be done on a small area and materials with delicate and complex structures, such as thin films and coatings [10]. Furthermore, a vast number of properties can be generated from the nanoindentation data, such as elastic modulus, hardness, creep, fracture toughness, H-E ratios, and stiffness of materials [11]. These payoffs make nanoindentation an obvious choice for this study.

Based on reported literature, the wear behaviour and nanoindentation properties of spark plasma sintered TiAl alloys are scarcely discussed. This work focuses on wear and nanoindentation creep and fracture toughness properties of $Ti_{48}Al_{48}Cr_2Nb_2$ alloy fabricated using spark plasma sintering. The microstructure evolution and wear performance of the alloy are conferred.

2. EXPERIMENTAL

Ti-based alloys were fabricated using the pre-alloyed gas-atomized powder with a nominal chemical composition of (at.%) $Ti_{48}Al_{48}Cr_2Nb_2$, supplied by TLS-Technik. The nominal composition and basic elemental properties are provided in Table 1. The average particle size of the powder was in the range of <36μm. TiAl powder material was consolidated using a spark plasma sintering system, HHPD-25 FCT type SPS machine. The sintering temperature (T) was 1200 °C, with a heating rate (HR) of 50 °C/min and 100 °C/min and holding time (HT) of 5 min and 7.5 min, at a constant pressure of 50 MPa. Samples were 20 mm in diameter and 5 mm thick and were subsequently metallographically prepared for microstructural analysis using standard procedures [12] to obtain a mirror surface finish. The microstructure was examined afterward using scanning electron microscopy - backscattering electron (JEOL JSM-7900F) equipped with electron dispersive X-ray spectroscopy (EDS).

Table 1. Nominal composition and basic properties of the elements.

Composition	at.%	Density (g/cm3)	Hardness (GPa)	Elastic modulus (GPa)
Ti	48	4.54	3.4	116
Al	48	2.7	0.35	76
Cr	2	7.19	1.06	279
Nb	2	8.57	1.32	170

Dry sliding wear tests were conducted using a ball-on-disk tribometer TRB3 by Anton Paar, with respect to the ASTM G99-05. Hardened counterface steel of 60 HB was used in all the tests. For all samples, tests were carried out for about 9540 cycles covering a distance of 600m over a radius of 10mm with an applied force of 10 N. The tests were repeated three times to ensure the reliability of the data. The weight of the samples was recorded before and after each test, and the difference in the weighed mass was used to determine the wear volumes of the samples.

Wear surface morphologies were examined using scanning electron microscopy - backscattering electron (JEOL JSM-7900F). Depth, width, and surface roughness were analyzed using a profilometer (Taylor Hobson Surtronic 128). An average of three 2D profiles were taken along the wear track. Thereafter, average wear area loss, $\overline{A}_w$ (cm²) was calculated by accounting for the depth (Y) and width (X) values obtained from the 2D profiles according to the equation 1 [13].

$$\overline{A}_w = \sum_{i-0}^{n} 0.5\,(Y_i + Y_{i-1})(X_i - X_{i-1}) \qquad (1)$$

Average depth, $\overline{D}$ (cm), can be calculated by considering $\overline{A}_w$ and the average wear track width ($\overline{W}$) via equation 2 [13].

$$\overline{D} = \frac{\overline{A}_w}{\overline{W}} \qquad (2)$$

Volume loss, V (cm³) was calculated according to equation 3 [13].

$$V = \left[\frac{1}{3} \cdot \pi \overline{D}^2 (3R - \overline{D})\right] + \overline{A}_w \cdot l \qquad (3)$$

where R is the radius of the alumina steel ball (6 mm), and l is the total stroke radius (10 mm). Lastly, the wear rate, W_v (cm³/m) was calculated by accounting for the V and the applied load, F_N (N) through equation 4 [13].

$$W_v = \frac{V}{S} \qquad (4)$$

Microhardness tests were performed using digital microhardness (INNOVATEST Falcon 500), by making an array of a minimum of 10 indents on the samples. The applied load was kept at 10 kg for all tests and held at peak load for about 10 s. The diagonals of the resultant indents were then measured to obtain the material hardness values with an accuracy of ±10 μm.

Nanoindentation properties were determined using UNHT nanoindenter by Anton Paar. A minimum of 10 indents were done on the samples using a force control at an applied load of 100mN and 10 s dwell time. Yield stress was calculated considering hardness (H) according to the Tabor relationship given in equation 5 [14].

$$\sigma_y = \frac{H}{3} \qquad (5)$$

Fracture toughness can be estimated using equation 6 and 7 [15].

$$K_{IC} = 0.079 \left(\frac{P}{a^{1.5}}\right) \log\left(4.5 \cdot \frac{a}{c}\right) \text{ MPa m}^{0.5} \qquad (6)$$

$$K_{IC} = \alpha \left(\frac{E}{H}\right)^{0.5} \left(\frac{P}{C^{1.5}}\right) \qquad (7)$$

where a or α is the diagonal half indentation which is approximately 0.04 for the Berkovich indenter [16]. P is the applied load normal to the stress, and c is the crack length and half indentation diagonal.

The indentation creep (C_{IT}) can be described as the percentage increase in indentation depth under constant applied load over a set time. C_{IT} was determined using the equation 8 [17].

$$C_{IT} = \left[\frac{(h_2 - h_1)}{h_1}\right] \cdot 100\% \qquad (8)$$

Where h_1 and h_2 represent indentation depth at t_1 and t_2 at maximum holding force, respectively.

3. RESULTS AND DISCUSSIONS

3.1 Densification of TiAl-based powders

The SEM backscattered electron image and corresponding elemental dispersive spectroscopy (EDS) analysis of the elemental composition of the $Ti_{48}Al_{48}Cr_2Nb_2$ powder used for the study are shown in Figure 1 (a, b & c). The SEM examination (Figure 1a) clearly showed a fine composite structure of the TiAl powder with spherical particles. The grain sizes are estimated to be in the range of 5- 45μm. Based on the EDS peaks of the different elements, the presence of the following elements, Ti-Al-Cr-Nb, is confirmed. Minor trace elements of Th, Er, Sc, N, and Br can be observed on the EDS graph, which could have resulted from the atomization powder production process.
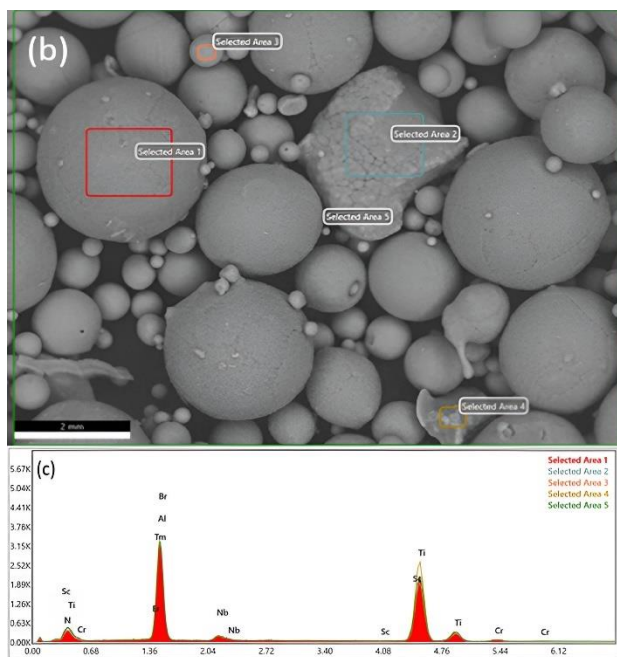

501
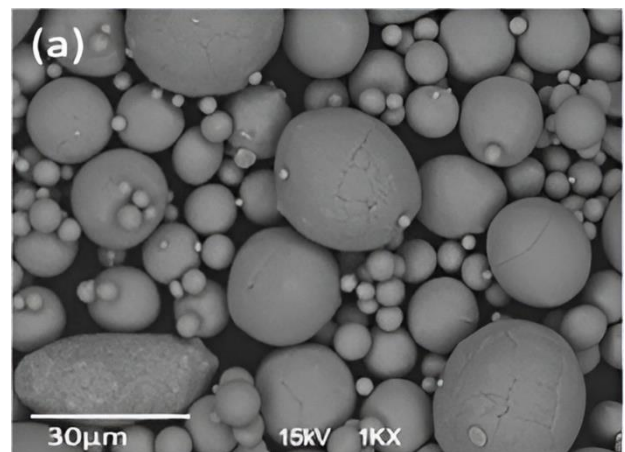
Fig. 1. (a) SEM backscattered electron image of the TiAl powder, (b & c) SEM-EDS analysis of the TiAl powder.

Table 2 shows the densities of the $Ti_{48}Al_{48}Cr_2Nb_2$ alloy spark plasma sintered at 1200 °C for 5 and 7.5 min with a heating rate of 50 °C and 100 °C under the pressure of 50 MPa in a vacuum environment.

Table 2. Relative density of Ti-48Al-2Cr-2Nb alloy spark plasma sintered at 1150°C, 1175°C, and 1200°C.

Sintering conditions	Relative densities (%)
1200°C 5min-50°C/min	96
1200°C 7.5min-50°C/min	98
1200°C 5min-100°C/min	95
1200°C 7.5min-100°C/min	97

High densification of 98% and 97% were achieved for alloys sintered for 7.5 mins with a heating rate of 50 °C/min and 100 °C/min, respectively. Holding time of 7.5 mins ensured increased interaction of particles and depletion of voids between particles, thus resulting in increased densities. Slightly lower densification of 96% and 97% occurred after 5 min of sintering with heating rates of 50 °C/min and 100 °C/min, respectively. This decrease in densities could be related to the use of a combination of low pressure and short sintering time, which limited densification. A previous study [18] showed that at a short sintering time, the application of high pressure in SPS of the TiAl alloy is effective for yielding well-densified samples as a density of ~99% was attained sintering using the pressure of 80MPa and temperature of 1100°C for 4mins.

High applied pressure assists in breaking powder agglomerates and encourages high contact of particles, thus accelerating the migration of atoms even at low temperatures.

3.2 X-ray diffraction analysis

X-ray diffraction (XRD) patterns of the TiAl alloys sintered at different sintering parameters are illustrated in Figure 2. Results indicated the presence of 2 major crystalline phases, γ-TiAl, and $Ti_3Al_{2.25}Nb_{0.75}$, and other minor precipitated phases such as β-Ti (Beta-titanium), TiN (Titanium nitride), NbC (Niobium carbide) and β-CrOOH (Orthorhombic guyanaite) in all sintered samples. It is observed that all four sintered samples displayed similar diffraction patterns. This could indicate that the sintering parameters used do not result in structural changes.
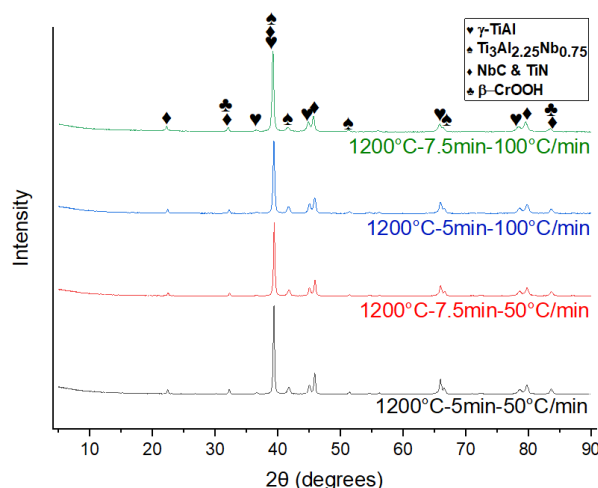

Fig. 2. X-ray diffraction analysis of the TiAl alloys produced at sintering T of 1200 °C, HT of 5min and 7.5min, and HR of 50 °C/min and 100 °C/min.

3.3 Microstructure characteristics

SEM-backscatter microstructural information of samples spark plasma sintered at 1200 °C at the varied heating rate and holding time is presented in Figure 3(a-d). In Figure 3a, a sample sintered for 5 min with a heating rate of 50°C/min showed a coarse, fully lamellar structure consisting of alternating plates of α_2 and γ plates and is reported to have a typical size range of 200 μm – 1000μm [19]. When the heating rate was increased to 100 °C/min, the sintered sample displayed a duplex-structure with coarse lamellar colonies and equiaxed grain in the average size range of 10 μm, as shown in Figure 3b. For the sample sintered for 7.5min at a heating rate of 50 °C/min, Figure 3c, the

longer sintering time resulted in microstructure coarsening of the grains and the change of the microstructure to the nearly lamellar structure consisting of large volumes of lamellar colonies with the average size of about 100 μm and slight amounts of equiaxed gamma grains having an average grain size of 10 μm. When the heating rate was changed from 50 °C/min to 100 °C/min, the sintered sample exhibited a very fine duplex structure consisting of a near gamma structure (Figure 3d) with fine lamellar colonies and equiaxed gamma grains in the size range 5 μm – 10 μm and is characterized by α_2 precipitates dispersed at the grain boundaries [20]. The micrographs depict the effect of sintering time and heating rate on the microstructure of the sintered samples. Thus, the composition and synthesis process greatly influence the evolution of these microstructures. The $Ti_{48}Al_{48}Cr_2Nb_2$ alloy structure ranges from those composed of fine equiaxed γ-grains in a matrix of α_2 to those consisting of fully lamellar (γ+α_2) polycrystalline aggregates, which are sensitive to its microstructure, grain-size and small volumes of alloying constituents [21].
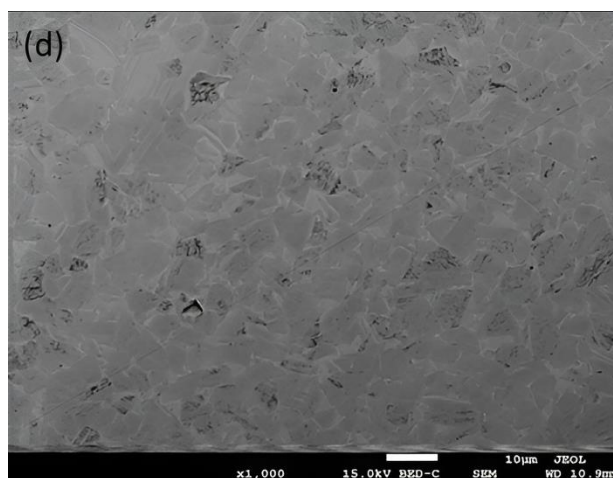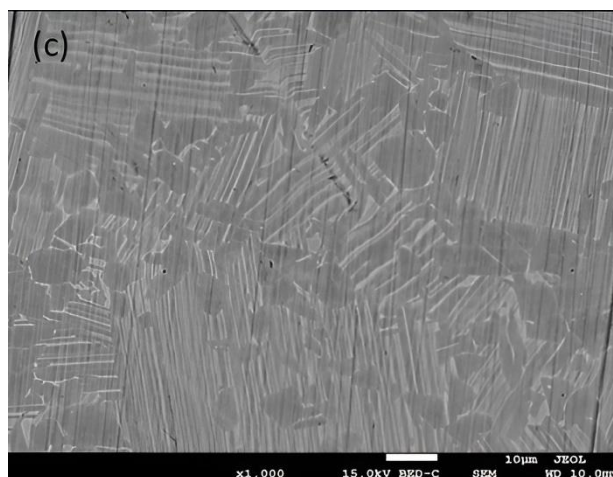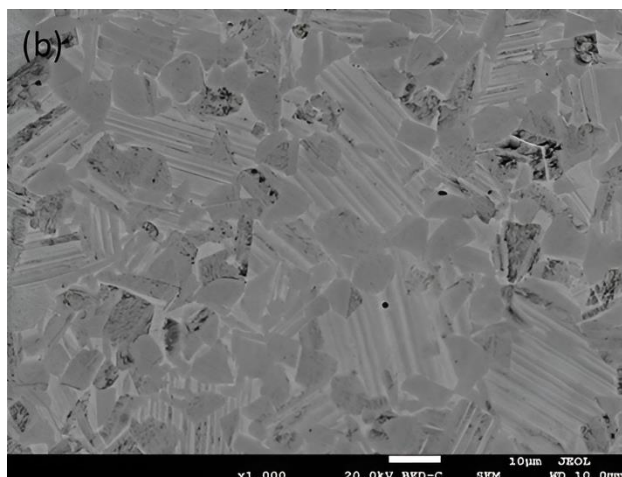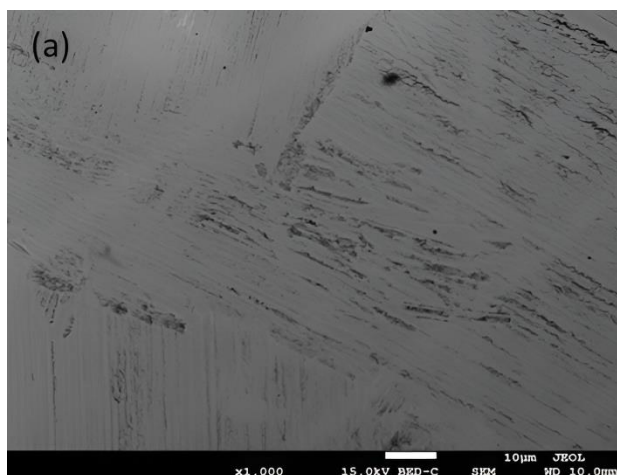

Fig. 3. (a) SEM back-scattered images of TiAl alloys sintered at 1200°C-5min-50°C/min, (b) SEM back-scattered images of TiAl alloys sintered at 1200°C-5min-100C/min, (c) SEM back-scattered images of TiAl alloys sintered at 1200°C-7.5min 50°C/min, (d) SEM back-scattered images of TiAl alloys sintered at 1200°C-7.5min-100°C/min.

3.4 Hardness, elastic modulus, and volume material loss of TiAl Alloy

The Microhardness, nanohardness, and elastic modulus of the samples sintered at varied conditions are shown in Table 3. The results showed that the hardness values and the elastic modulus are affected by the sintering conditions. An obvious correlation between microhardness and nanohardness was also established. Samples sintered for 5 min showed the least microhardness values of 3.17 GPa and 3.42 GPa and nanohardness values of 3.6705 and 3.7429 GPa for the samples sintered using a heating rate of 50 °C and 100 °C respectively. This reduced hardness in the materials may be associated with the duration of sintering which limited the degree of densification (refer to Table 2) for the samples

due to the restricted particles' contact time during the SPS processing of the TiAl powders. In addition to the time limitation, the slow heating rate of 50 ℃/min resulted in the lowest hardness in the sample sintered for 5 min with a heating rate by contributing to grain coarsening in the microstructure (fully lamellar, Figure 2a). Reported studies show that samples that are processed slowly have coarsened grain size compared to their fast-processed counterparts [22]. Furthermore, the lamellar structure is characterized by low strength [23] but at the expense of strength. The sample having a microhardness hardness of 3.42 GPa and nanohardnes of 3.7429 GPa showed a duplex structure (Figure 2b) which is associated with good strength [24].

On the other hand, samples sintered for a slightly longer duration of 7.5 min showed improved hardness of 4.429 GPa and 3.924 GPa for the samples sintered using a heating rate of 50 ℃and 100 ℃, respectively. Similarly, high nanohardness of 4.0012 and 3.7463 GPa was observed on the same samples, respectively. The observed high hardness correlates with the good densification of 98% and 97% of the samples, respectively, presented in Table 2.

Table 3. Microhardness, Nanohardness, and Elastic Modulus of the TiAl samples sintered at 1200°C.

Sintering Conditions	Microhardness (GPa)	Nanohardness (GPa)	Elastic Modulus (GPa)
5min-50°C/min	3.17	3.6705	28.81
7.5min-50°C/min	4.429	4.0012	31.0234
5min-100°C/min	3.42	3.7429	29.069
7.5min-100°/min	3.924	3.7463	29.133

The slightly longer duration might have contributed to the increase in hardness by encouraging good densification by allowing more time for particle interaction and pore closure. Long sintering time increases the relative density as diffusion of atoms between compacted powder has adequate time to occur [25]. The high hardness of the samples sintered for 7.5 min at the heating rate of 50 ℃can also be attributed to the nearly lamellar structure (Figure 2c), which is characterized by good strength, in addition to good ductility and creep resistance provided by duplex structure as a result of the ductile lamellar

colonies and a fraction of hard small equiaxed grains [26]. Additionally, a clear link between hardness and elastic modulus was observed, as an increase in hardness resulted in an increase in elastic modulus. This detected relationship confirms the intrinsic practical dependency of elastic modulus on hardness as alluded to by Cheng and Cheng [27].

3.5 Yield stress and fracture toughness

The results shown in Figure 4 indicate the mean variation yield stress and fracture toughness of the sintered alloys as estimated using data from nanoindentation tests.
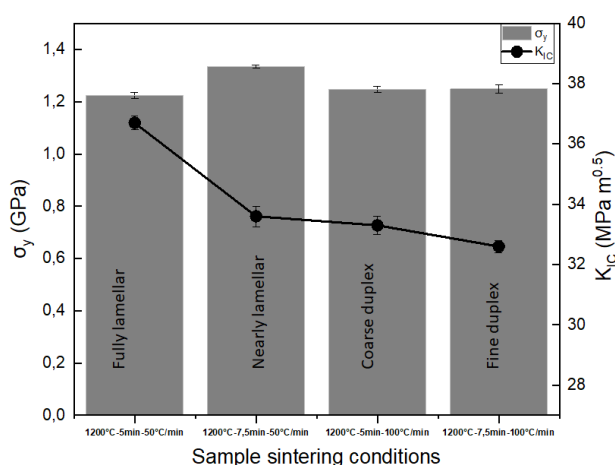

Fig. 4. Yield stress and Fracture toughness of the sintered TiAl alloys exhibiting varying microstructural features.

A non-linear relationship was observed between the yield stress (σ_y) and the fracture toughness (K_{IC}) in which the σ_y increases with a decrease in K_{IC}. The variations in the σ_y and K_{IC} in all the samples were attributed to the difference in the microstructural features observed in Figure 2. High fracture toughness is observed in the sample having a fully lamellar structure although it recorded slightly less yield stress. Fully lamellar structure is characterized by high crack growth thresholds with a recorded value of about 37 MPa m$^{0.5}$. Previous studies have linked improved fracture toughness of the lamellar microstructures to crack deflection and branching, crack tip blunting in the α_2 phase, and slip and twinning in the γ phase [28]. On the contrary, duplex microstructure exhibited reduced fracture toughness because of the detrimental effect of the equiaxed morphology (i.e., fine equiaxed grains) which tends to reduce crack growth resistance. Thus, a slight reduction

in K_{IC} can be observed in the fine duplex structure in comparison to the coarse duplex structure, from 33 and 32.5 MPa m0.5, which is characterized by a relatively large number of lamellar colonies, whilst demonstrating a similar σ_y of about 1.24 GPa. This behaviour is consistent with previous reports which suggest that lamellar structures exhibit superior K_{IC} to those of duplex structures [28, 29].

3.6 Creep deformation behaviour

Nanoindentation offers the advantage of being able to extract material properties, such as creep response, from a single nanoindentation test. Figure 5 depicts the nanoindentation time-dependent creep deformation curves. The materials showed a progressive deformation under constant load over time. A maximum indentation depth of around 1450 nm within 45 s before unloading was reached in the samples, except for the sample sintered for 7.5 min at a heating rate of 50 °C/min which recorded an indentation depth of around 800 nm. The stark difference in creep for the sample can be attributed to the constituent lamellar colonies with average size of about 150 μm and slight amounts of equiaxed gamma grains of 10 μm. These microstructural features contribute to the ease of dislocation mobility leading to the combined pinning effect by dislocation entanglement and equiaxed grains thereby imparting enhanced creep resistance. Materials having a great number of grains are thought to experience significant grain boundary sliding creep as opposed to those with fewer grains [14].
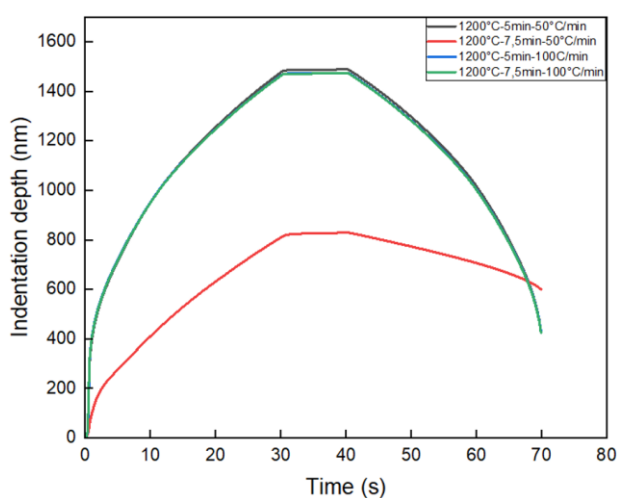

Fig. 5. Nanoindentation creep deformation as a function of time.

3.7 Coefficient of friction and wear rate

Figure 6 illustrates the variation of the averaged coefficient of friction (COF) and specific wear rates as a function of load (10N) for the sintered $Ti_{48}Al_{48}Cr_2Nb_2$ alloys in sliding contact with a steel ball. The COF for all the samples ranges from 0.436 to 0.523.
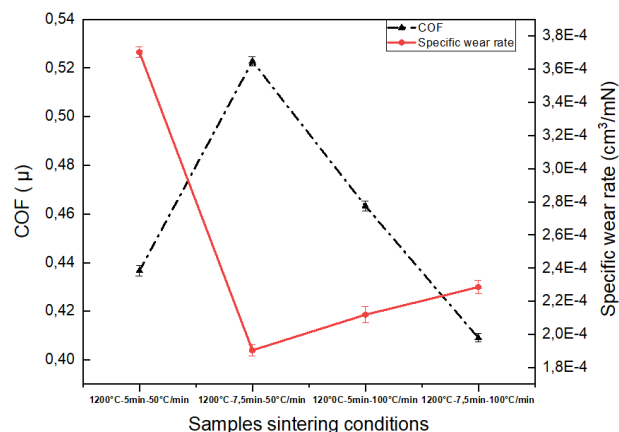

Fig. 6. Mean values of COF and Specific wear rates for $Ti_{48}Al_{48}Cr_2Nb_2$ for the 10N applied load.

The COF variation could be attributed to the presence of wear debris particles generated when the counterface steel ball slides over the sintered TiAl samples. Additionally, it can be postulated that any open pores and their distributions on the surface contributed to the observed variation in the COF. It can be seen that there is no apparent trend in the COF with respect to the specific wear rates of the different samples. However, an obvious reduction in the specific wear rate was observed for alloys sintered for 7.5 min and alloys sintered with a heating rate of 100 ℃ The observed decrease in the specific wear rates indicates that the heating rate and holding time contribute to the densification of the material during the sintering processes. Additionally, the good tribological properties could be credited to the lamellar and equiaxed grain phase mixture, resulting in good wear resistance due to the dislocation pinning effect of the equiaxed grains. On the contrary, the sample sintered with a heating rate of 50 ℃/min and a hold time of 5 min showed a high specific wear rate credited to the low densification (96%) and the fully lamellar microstructural properties of these alloys. On the other hand, the sample sintered with a heating rate of 100 ℃/min for 7.5 min while it had low densification (95%); it presented a duplex (lamellar colonies + equiaxed grains) microstructure. The equiaxed structure is known to

exhibit resistance to deformation due to its hardened nature resulting from its relatively refined grains. In contrast, the lamellar structure presents a ductile behaviour due to the large and long colonies.

Specific wear rates of the alloy sintered with various holding times and the heating rate at 1200 °Care presented as a function of H/E ratios are depicted in Figure 7.
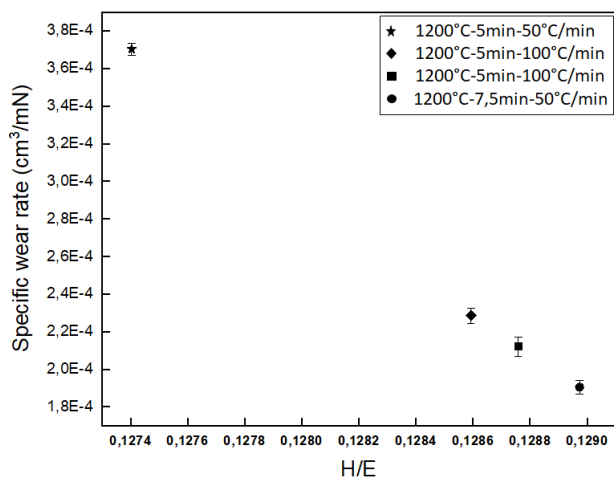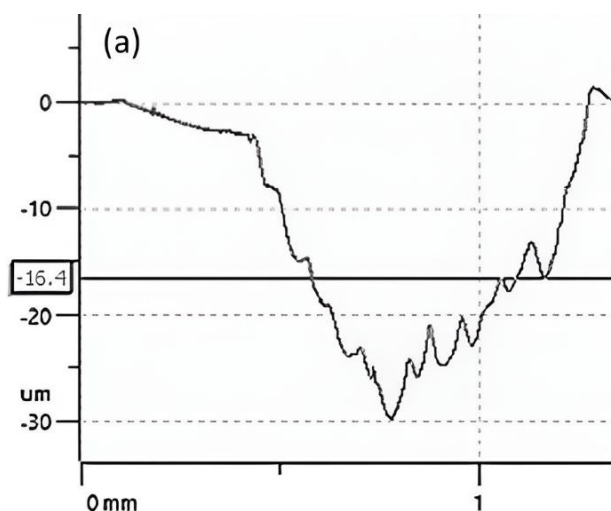

Fig. 7. The relationship between the mean specific rate and H/E ratio of the TiAl alloy processed under different sintering conditions.

The most significant specific wear rate was recorded for the sample sintered with a heating rate of 50°C/min and a holding time of 5min due to low hardness (Table 3) and the ductile nature imposed by the coarsened fully lamellar structure of this material. This mainly is because the material deformation behaviour of lamellar microstructure can be affected by its grain size, as well as other microstructural features such as the lamellar orientation, lamellar spacing, and thickness [30], with coarser lamellar structures being more prone to deformation. At the same time, the least specific wear rate was demonstrated by the sample produced with a heating rate of 50°C and a holding time of 7.5 min due to having excellent hardness achieved by good densification of the material during the sintering process. Furthermore, the presence of Nb in the form of the carbide NbC in γ-TiAl and α2-Ti3Al phases (Figure 3) limits material softening by the process of strain hardening [2] since it's a wear-resistant hard phase [31] which also acts as a grain refiner. Furthermore, a direct link between the wear and H/E ratio was established. The plot shows a tendency of wear to decrease with an increase in the value of *H/E*. Thus,

it may be concluded that the specific wear rate shows a good correlation with the values of *H/E*. Obtained higher H/E ratio (~0.1290) indicates the material's better resistance to wear associated with plastic deformation.

3.8 Wear track profilometer measurements

Line profiles of the worn surfaces of the TiAl are shown in Figure 8 a-d. The materials showed a variation in depth and width, indicating the influence of processing parameters on the wear behaviour of the TiAl materials. Sample sintered for 5 min at 50 ℃/min showed higher wear rates and material loss, as evidenced by the broader and deeper wear track depicted in Figure 8a. It can be observed that the samples sintered for the same duration but at a different heating rate of 100 ℃ exhibited a deeper wear track, as portrayed in Figure 8b. However, its width was relatively narrow; hence the material experienced a slight decrease in the wear rate. Reduced wear rates are observed in the materials sintered for 7.5 min, as shown in Figure 8c-d, and the samples sintered using a heating rate of 50 ℃/min showed the minor wear rate, as evidenced by the shallow and narrow wear track. Corresponding surface roughness (Ra) and mean width profile (RSm) of the TiAl samples' worn surface are displayed in Figure 9 and range between 2.24 μm and 2.281 μm, respectively. Both samples sintered for 7.5 min at the heating rate of 50 ℃/min and 100 ℃/min recorded the least Ra of about 2.24 μm, over a mean width profile of about 270 μm and 256 μm, respectively. The reduction in Ra could be ascribed to the samples' low porosity, thus causing reduced surface friction. This implies that diminished surface porosity decreases COF and enhances tribological performance.
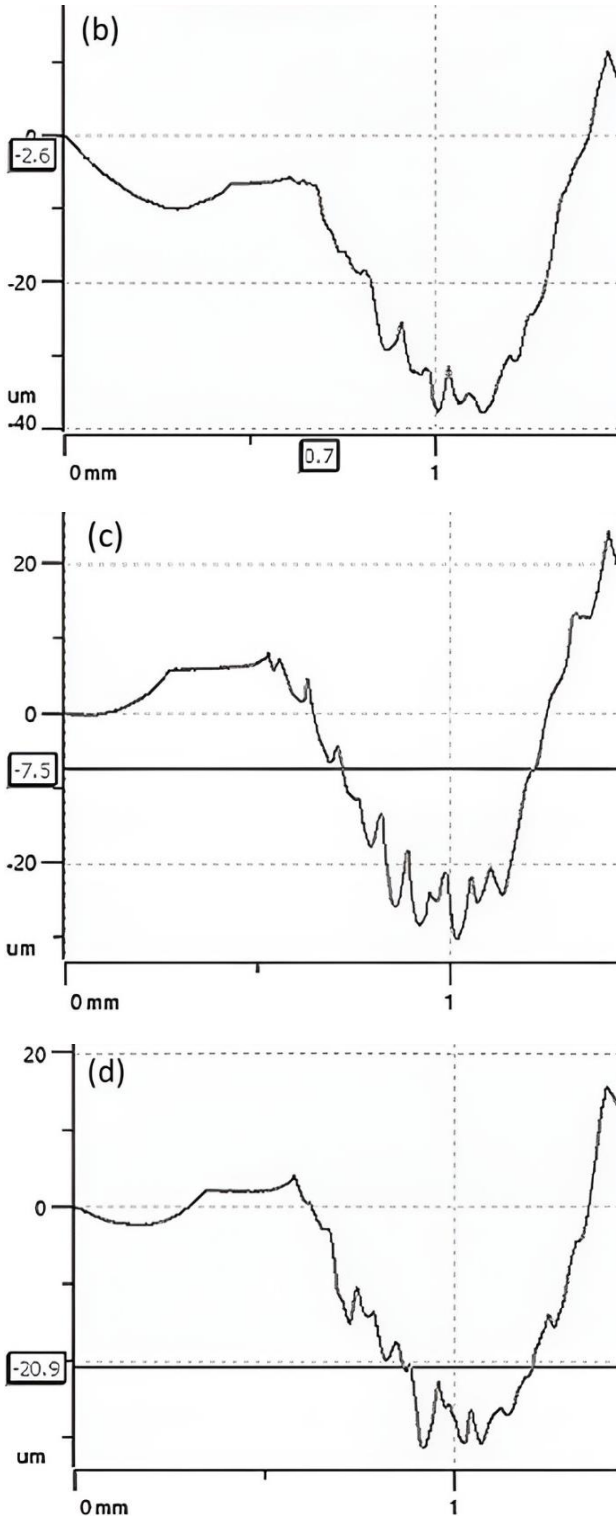
Fig. 9. Surface roughness and profile mean width of the TiAl samples' worn surface.

3.9 Wear track morphology analysis

The wear tracks of the TiAl alloys were studied by SEM at higher magnification to reveal surface features and to understand the wear mechanisms involved. Figure 10 (a-d) shows the wear track images on the sintered TiAl alloy. The presence of abraded regions, accumulation of fine debris particles, and parallel grooves suggest that the samples underwent an abrasive wear mechanism.

Fig. 8. (a) Profilometer profiles of the wear track depth on the TiAl alloys sintered at 1200°C-5min-50℃/min, (b) Profilometer profiles of the wear track depth on the TiAl alloys sintered at 1200°C-5min-100℃/min, (c) Profilometer profiles of the wear track depth on the TiAl alloys sintered at 120°C-7.5min-50℃/min, (d) Profilometer profiles of the wear track depth on the TiAl alloys sintered at 1200°C-7.5min-100℃/min.
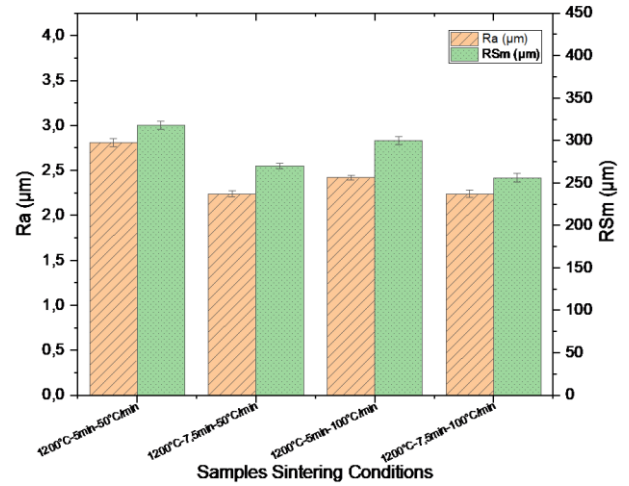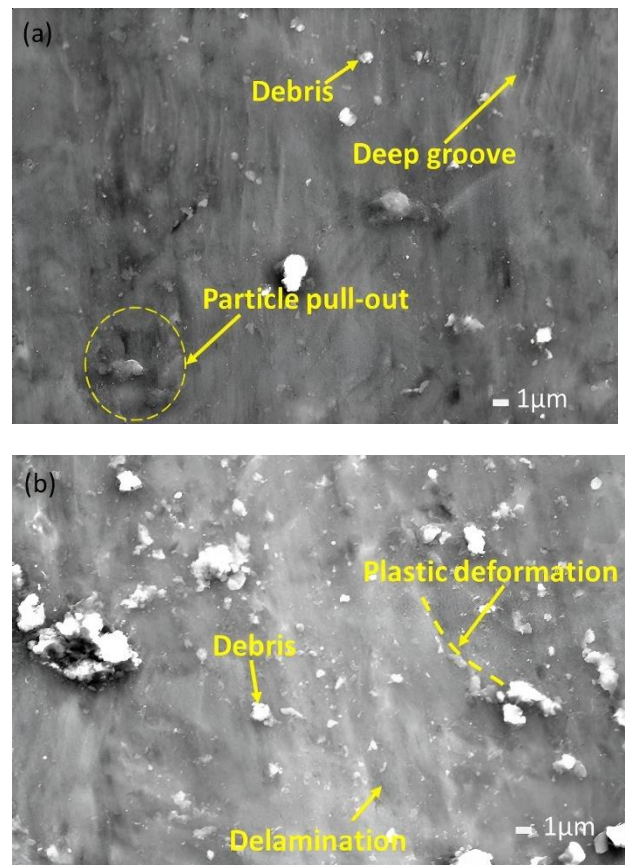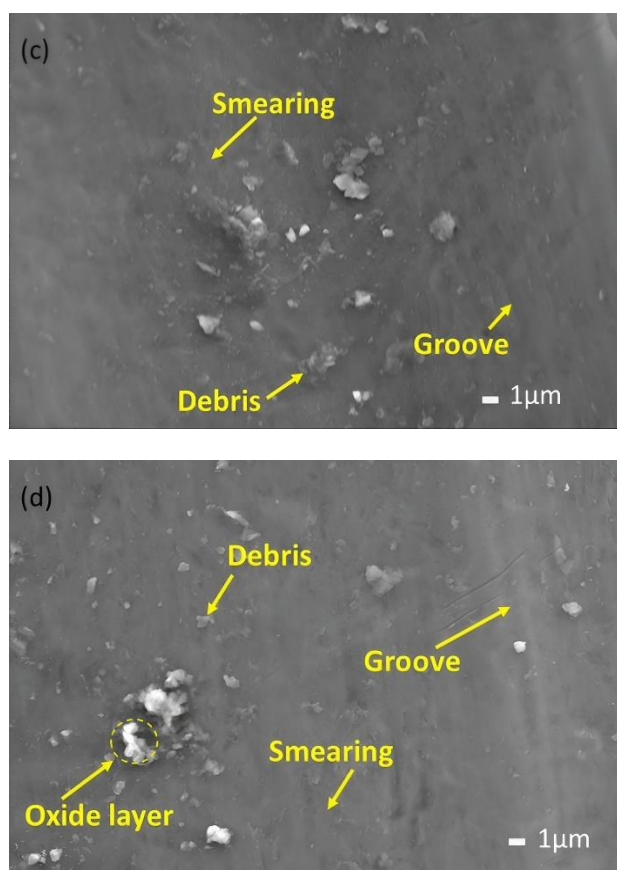
Fig. 10. (a) SEM analysis of wear tracks of TiAl alloys sintered at 1200℃-5min-50℃/min, (b) SEM analysis of wear tracks of TiAl alloys sintered at 1200℃-5min-100℃/min, (c) SEM analysis of wear tracks of TiAl alloys sintered at 1200℃-7.5min-50℃/min, (d) SEM analysis of wear tracks of TiAl alloys sintered at 1200℃-7.5min-100℃/min.

However, samples sintered for 5 mins as shown in Figures 10a and 10b, were characterized by a large amount of surface damage evidenced by particle pull-out and plastic deformation, respectively. This behaviour is linked to poor resistance to penetration by a counter-body as evidenced by the deeper grooves on the worn surface. Conversely, samples sintered for 7.5 min, as presented in Figures 10c and 10d, showed significant formation of smearing with no significant plowing on the worn surfaces indicating that the adhesive wear mechanism was also at play. This observed resistance to deformation in the samples sintered for 7.5 min could be attributed to the superior hardness of the material, as presented in Table 3. Largely, the wear indicates an adhesive–abrasive mechanism, with a predominantly adhesive wear mechanism.

4. CONCLUSION

TiAl alloy spark plasma sintered at 1200 °C using varied heating rates (50 ℃/min and 100 ℃/min) and holding times (5 min and 7,5 min) were studied for their tribological behaviour.

1. Microstructural features of the TiAl alloys showed to be sensitive to sintering time and heating rate.

2. The nearly lamellar structure exhibited good wear resistance properties.

3. The morphology of the worn surface indicated that both adhesive and abrasive wear mechanisms were responsible for the wear of the alloys.

4. Abrasive wear dominated on the samples sintered for 5 min, resulting in significant damage to the surface and excessive wear.

5. The sample produced at a heating rate of 50 °C/min and a holding time of 7.5 min showed a higher sintered density of about 98% and high hardness, resulting in improved wear resistance and lower coefficient of friction.

6. Fracture toughness, yield stress, and creep deformation were shown to be significantly influenced by microstructural morphologies. The fully lamellar microstructure yielded better fracture toughness of about 36.7 MPa $m^{0.5}$ with a yield stress threshold of about 1.22 GPa. The nearly lamellar microstructure showed decreased fracture toughness of about 33.6 MPa $m^{0.5}$ but yielded improved yield stress of about 1.3 GPa and better resistance to creep deformation compared to other microstructures. Variations in fracture toughness and creep deformation for the different microstructures may offer viable design considerations for engineering structures.

7. Specific wear rate of the material showed a dependency on the H/E ratio and provides useful information on the resistance of a material to wear.

8. Profiles of the wear tracks confirmed the degree of wear on the samples by revealing their depth and width. A shallow and narrow width was noticed in the sample sintered at 50 °C/min and a holding time of 7.5min which corroborated the wear resistance of the sample.

9. As TiAl alloy is applicable in wear-intensive components such as turbine blades, their tribological behaviour must be understood for developing and improving the material to ensure the longevity of design structures in-service.

ORCID iDs

Mahlatse R. Mphahlele 0000-0002-5527-0679
Peter A. Olubambi 0000-0002-2013-1724
Eugene Olevsky 0000-0002-0026-1935

REFERENCES

[1] B. Prayoga, S. Suyitno, and R. Dharmastiti, "The wear behavior of UHMWPE against surface modified cp-titanium by thermal oxidation," *Tribology in Industry*, vol. 38, no. 4, pp. 543-551, Dec. 2016.

[2] A. Ismaeel and C.-S. Wang, "Effect of Nb additions on microstructure and properties of γ-TiAl based alloys fabricated by selective laser melting," *Transactions of Nonferrous Metals Society of China/Transactions of Nonferrous Metals Society of China*, vol. 29, no. 5, pp. 1007–1016, May 2019, doi: 10.1016/s1003-6326(19)65009-0.

[3] L. Wang *et al.*, "Achieving the excellent self-lubricity and low wear of TiAl intermetallics through the addition of copper coated graphite," *Composites. Part B, Engineering*, vol. 198, p. 108223, Oct. 2020, doi: 10.1016/j.compositesb.2020.108223.

[4] T. Penyashki, et al., "Some ways to increase the wear resistance of titanium alloys," *Journal of the Balkan Tribological Association*, vol. 27, no. 1, pp. 1-20, Mar. 2021.

[5] A. S. Wadhwa and A. Chauhan, "An overview of the mechanical and tribological characteristics of non - ferrous metal matrix composites for advanced engineering applications," *Tribology in Industry*, vol. 45, no. 1, pp. 51–80, Mar. 2023, doi: 10.24874/ti.1359.08.22.12.

[6] M. Eriksson, M. Radwan, and Z. Shen, "Spark plasma sintering of WC, cemented carbide and functional graded materials," *International Journal of Refractory & Hard Metals*, vol. 36, pp. 31–37, Jan. 2013, doi: 10.1016/j.ijrmhm.2012.03.007.

[7] A. Miriyev, A. Levy, S. Kalabukhov, and N. Frage, "Interface evolution and shear strength of Al/Ti bi-metals processed by a spark plasma sintering (SPS) apparatus," *Journal of Alloys and Compounds*, vol. 678, pp. 329–336, Sep. 2016, doi: 10.1016/j.jallcom.2016.03.137.

[8] L. H. Liu *et al.*, "Ultrafine grained Ti-based composites with ultrahigh strength and ductility achieved by equiaxing microstructure," *Materials in Engineering*, vol. 79, pp. 1–5, Aug. 2015, doi: 10.1016/j.matdes.2015.04.032.

[9] A. Bhaduri, *Mechanical properties and working of metals and alloys*. 2018. doi: 10.1007/978-981-10-7209-3.

[10] W. C. Oliver and G. M. Pharr, "An improved technique for determining hardness and elastic modulus using load and displacement sensing indentation experiments," *Journal of Materials Research/Pratt's Guide to Venture Capital Sources*, vol. 7, no. 6, pp. 1564–1583, Jun. 1992, doi: 10.1557/jmr.1992.1564.

[11] M. Dada, P. Popoola, N. Mathe, S. Adeosun, and S. Pityana, "Investigating the elastic modulus and hardness properties of a high entropy alloy coating using nanoindentation," *International Journal of Lightweight Materials and Manufacture*, vol. 4, no. 3, pp. 339–345, Sep. 2021, doi: 10.1016/j.ijlmm.2021.04.002.

[12] K. Geels, D. Fowler, W. Kopp, and M. Rückert, *Metallographic and materialographic specimen preparation, light microscopy, image analysis and hardness testing*. 2007, doi: 10.1520/mnl46-eb.

[13] C. Chirico, A. V. Romero, E. Gordo, and S. A. Tsipas, "Improvement of wear resistance of low-cost powder metallurgy β-titanium alloys for biomedical applications," *Surface & Coatings Technology/Surface and Coatings Technology*, vol. 434, p. 128207, Mar. 2022, doi: 10.1016/j.surfcoat.2022.128207.

[14] M. Hasnine, J. C. Suhling, B. C. Prorok, M. J. Bozack, and P. Lall, "Anisotropic mechanical properties of SAC solder joints in microelectronic packaging and prediction of uniaxial creep using nanoindentation creep," *Experimental Mechanics*, vol. 57, no. 4, pp. 603–614, Feb. 2017, doi: 10.1007/s11340-017-0258-2.

[15] M. Masanta, S. M. Shariff, and A. R. Choudhury, "Evaluation of modulus of elasticity, nano-hardness and fracture toughness of TiB_2–TiC–Al_2O_3 composite coating developed by SHS and laser cladding," *Materials Science and Engineering. A,* vol. 528, no. 16–17, pp. 5327–5335, Jun. 2011, doi: 10.1016/j.msea.2011.03.057.

[16] M. R. Ayatollahi and A. Karimzadeh, "Nano-Indentation measurement of fracture toughness of dental enamel," *International Journal of Fracture*, vol. 183, no. 1, pp. 113–118, Jul. 2013, doi: 10.1007/s10704-013-9864-x.

[17] M. N. Hassan, S. Zinelis, M. Hersberger-Zurfluh, and T. Eliades, "Creep, hardness, and elastic modulus of lingual fixed retainers adhesives," *Materials*, vol. 12, no. 4, p. 646, Feb. 2019, doi: 10.3390/ma12040646.

[18] Y. Xia, J. L. Zhao, and M. Qian, "Spark plasma sintering of TI-48AL-2CR-2NB alloy powder and characterization of an unexpected phase," *JOM*, vol. 71, no. 8, pp. 2556–2563, Jun. 2019, doi: 10.1007/s11837-019-03590-w.

[19] K. Kothari, R. Radhakrishnan, and N. M. Wereley, "Advances in gamma titanium aluminides and their manufacturing techniques," *Progress in Aerospace Sciences/Progress in Aerospace Sciences*, vol. 55, pp. 1–16, Nov. 2012, doi: 10.1016/j.paerosci.2012.04.001.

[20] H. Clemens and S. Mayer, "Design, processing, microstructure, properties, and applications of advanced intermetallic TIAL alloys," *Advanced Engineering Materials*, vol. 15, no. 4, pp. 191–215, Nov. 2012, doi: 10.1002/adem.201200231.

[21] F. Appel, M. Oehring, J. D. H. Paul, Ch. Klinkenberg, and T. Carneiro, "Physical aspects of hot-working gamma-based titanium aluminides," *Intermetallics*, vol. 12, no. 7–9, pp. 791–802, Jul. 2004, doi: 10.1016/j.intermet.2004.02.042.

[22] O. Guillon *et al.*, "Field-Assisted Sintering Technology/Spark Plasma Sintering: Mechanisms, materials, and technology developments," *Advanced Engineering Materials*, vol. 16, no. 7, pp. 830–849, Apr. 2014, doi: 10.1002/adem.201300409.

[23] M. Ya. Brun, G. V. Shakhanova, and I. V. Soldatenko, "Effect of lamellar structure parameters on the properties of titanium alloy VT3-1," *Metal Science and Heat Treatment*, vol. 28, no. 7, pp. 519–522, Jul. 1986, doi: 10.1007/bf00780646.

[24] M. Lamirand, J. -l. Bonnentien, S. Guérin, G. Ferrière, and J. -p. Chevalier, "Effects of interstitial oxygen on microstructure and mechanical properties of Ti-48Al-2Cr-2Nb with fully lamellar and duplex microstructures," *Metallurgical and Materials Transactions. A, Physical Metallurgy and Materials Science*, vol. 37, no. 8, pp. 2369–2378, Aug. 2006, doi: 10.1007/bf02586211.

[25] M. A. Almomani, A. M. Shatnawi, and M. K. Alrashdan, "Effect of Sintering Time on the Density, Porosity Content and Microstructure of Copper – 1 wt. % Silicon Carbide Composites," *Advanced Materials Research*, vol. 1064, pp. 32–37, Dec. 2014, doi: 10.4028/www.scientific.net/amr.1064.32.

[26] M. Peters, J. Hemptenmacher J. Kumpfert, C. Leyens. (2003, Jun 28). *Structure and properties of titanium and titanium alloys*, doi: 10.1002/3527602119.ch1.

[27] J. Chen and S. J. Bull, "Relation between the ratio of elastic work to the total work of indentation and the ratio of hardness to Young's modulus for a perfect conical tip," *Journal of Materials Research/Pratt's Guide to Venture Capital Sources*, vol. 24, no. 3, pp. 590–598, Mar. 2009, doi: 10.1557/jmr.2009.0086.

[28] Y. Zheng *et al.*, "Fracture toughness of the bimodal size lamellar O phase microstructures in Ti-22Al-25Nb (at.%) orthorhombic alloy," *Journal of Alloys and Compounds*, vol. 709, pp. 511–518, Jun. 2017, doi: 10.1016/j.jallcom.2017.03.184.

[29] X. Shi, W. Zeng, and Q. Zhao, "The effects of lamellar features on the fracture toughness of Ti-17 titanium alloy," *Materials Science and Engineering. A, Structural Materials: Proporties, Microstructures and Processing/Materials Science & Engineering. A, Structural Materials: Properties, Microstructure and Processing*, vol. 636, pp. 543–550, Jun. 2015, doi: 10.1016/j.msea.2015.04.021.

[30] H. Zhu, K. Maruyama, D. Y. Seo, and P. Au, "Microstructural stability of fine-grained fully lamellar XD TiAl alloys by step aging," *Metallurgical and Materials Transactions. A, ,* vol. 36, no. 5, pp. 1339–1351, May 2005, doi: 10.1007/s11661-005-0225-x.

[31] V. Lazić, et al., "Carbide type influence on tribological properties of hard-faced steel layer. Part I: theoretical consideration", *Tribology in Industry*, vol. 32, no. 2, pp. 11-20, 2010.